Nanoscale

Accepted Manuscript

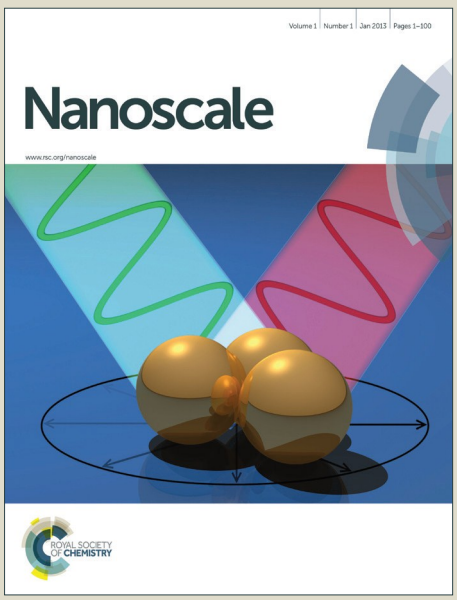

ROYAL SOCIETY OF CHEMISTRY

www.rsc.org/nanoscale

Nanoscale

RSCPublishing

ARTICLE

Polarization-Dependent Extraordinary Optical Transmission from Upconversion Nanoparticles

Cite this: DOI: 10.1039/xoxxoooooox

Peng Hui Wang,[a] Walter J. Salcedo,[b] Jothirmayanantham Pichaandi,[a] Frank C. J. M. van Veggel,[a] Alexandre G. Brolo[a*]

Received ooth January 2012,
Accepted ooth January 2012

DOI: 10.1039/xoxxoooooox

www.rsc.org/

Enhanced upconversion (UC) emission was experimentally demonstrated using gold nanoparticles double antennas coupled to nanoslits in gold films. The transmitted red emission from UC ytterbium and erbium co-doped sodium yttrium fluoride ($NaYF_4$:Yb^{3+}/Er^{3+}) nanoparticles (UC NPs) at ~665 nm (excited with a 980 nm diode laser) was enhanced relative to the green emission at ~550 nm. The relative enhanced UC NPs emission could be tuned by the different polarization-dependent extraordinary optical transmission modes coupled to the gold nanostructures. Finite-difference time-domain calculations suggest that the preferential enhanced UC emission is related to a combination of different surface plasmon modes excitation coupling to cavity Fabry-Perot interactions. A maximum UC enhancement of 6-fold was measured for nanoslits arrays in the absence of the double antennas. In the presence of the double nanoantennas inside the nanoslits, the UC enhancement was between 2 and 4-fold, depending on the experimental conditions.

1. Introduction

Extraordinary optical transmission (EOT) through metallic gratings, such as sub-wavelength holes and slits in thin metallic films, has been extensively studied[1-5] since first reported by Ebbesen[6] in 1998. The EOT phenomenon has been implemented in several applications, including bio-sensing,[7] beam focusing[8, 9], and enhanced photovoltaics. [10-12] Lanthanide-based upconversion (UC) emitters, which are capable of converting near-infrared radiation into visible luminescence, also attract much research attention due to their potential for novel applications. For instance, when used as biological labels, UC nanomaterials present low photo-bleaching and their near-infrared excitation (typically 980 nm) falls within the optical biological window, allowing long penetration depth in tissues.[13] UC materials can also be used in microlasers[14] devices and up-conversion solar cells.[15, 16] UC nano-materials, however, often have poor external quantum efficiency, due to their low absorption coefficient, parasitic processes and quenching.[17, 18] It has been demonstrated that UC nanoparticles (UC NPs) luminescence can be enhanced when coupled to metallic nanostructures through resonant energy transfer (ET) involving surface plasmons (SPs).[17, 19-21] The capability of engineering SP-active nanostructures[22] (geometry and surrounding dielectric) for enhanced UC EOT might have a potential for applications in photonics,[23, 24] and as sensitive single emitter detectors.[25-28]

In this work, polarized EOT from UC emissions were experimentally demonstrated by using Au double-antenna nanoparticles (DA NPs) nested in nanoslits in thin gold films. The roles of SP mode coupling and field confinement in the EOT process were evaluated.[29] It has been shown that the presence of nanoparticles chains inside nanoslits significantly affects light transmission relative to the slits without NPs.[2] However, the effect of nanoantennas (rather than nanoparticles) on the slit transmission and the interaction of those type of structures with emitter materials has not been explored. The presence of DA NPs inside nanoslits are expected to concentrate electromagnetic field in gap modes.[25, 30, 31] The nanoslits and DA NPs geometries were optimized to have their SP resonance overlapping with the UC NPs emission spectrum, facilitating the EOT at those wavelengths. The experimental

results show a maximum overall UC enhancement (relative to a window reference) of about 6-fold and an enhancement in the ratio between the transmitted UC red emission (~665 nm) and the green emission (~550 nm). The preferential enhanced UC NPs emissions were strongly polarization dependent and could be tuned by different EOT modes, as confirmed by FDTD calculations. This work then provides insights not only into the plasmonic enhancement mechanism for UC processes, but also on the different light transmission modes enabled by the nanostructures.

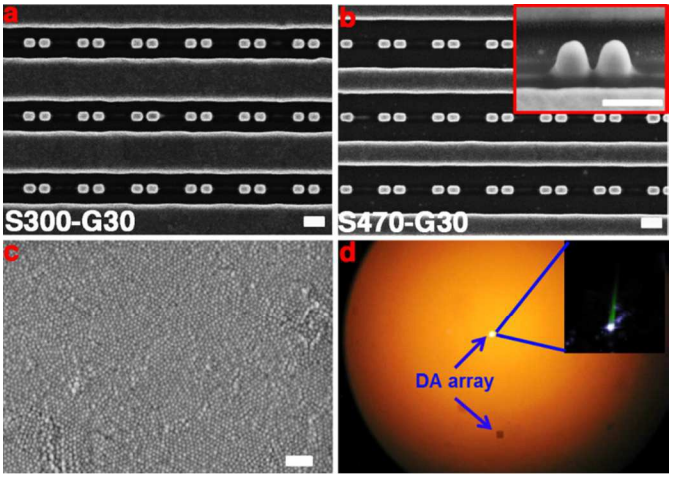

Figure 1 (a) and **(b)** SEM image top view of double antenna (DA) NPs structure inside a nanoslit: S300-G30 and S470-G30 respectively; the side view of a pair of DA is shown as an inset image (substrate titled at 45°). **(c)** UC NPs film covering a nanostructured array on the gold substrate. **(d)** Optical microscope image of UC NPs-covered arrays on a gold film. One of the arrays is illuminated by the 980 nm laser excitation (brighter spot). The insert shows an optical image of the UC emission from one of the arrays in the dark. Dimensions: scale bar **(a)**, **(b)** and **(c)** 200nm, **(d)** each nanostructured square array is about 11.6 x 11.6 μm^2.

2. Experimental Section

2.1 Fabrication of the Plasmonic Nanostructures

The nanostructures were fabricated on 100 nm gold film (5 nm Cr was used as adhesion layer) deposited on 1 mm thick glass slide (commercially available from EMF, Ithaca, NY) by focused-ion-beam (FIB) milling. In general, the gallium ion beam was set with 40 KeV at 12K magnification and the dwell time for each pixel was 5 µs. Two kinds of slits: 300 nm and 470 nm slit opening width (named as S300 and S470, respectively) were fabricated. The dimensions (length x width x height) of the DA NPs were 120 x 80 x 100 nm^3 (characterized by scanning electron micrographs (SEM) images, as shown in the inset of Figure 1b). DA NPs were fabricated in the center of the slits with different DA NPs gap distances: 14, 30, 120 and 180 nm, respectively (measured from SEM images, named as G14, G30, G120 and G180). SEM of all structures are shown in Figure 1 and as electronic supplementary information† (ESI) in Figure SI-1 and Figure SI-2. The distance between two DA NPs dimers was kept constant at 250 nm. The slit periodicity was also kept constant at 700 nm. In addition, control samples consisting of 80 nm-width Au lines (instead of DA NPs) inside the slits (S300-Line) and empty slits (S) were also fabricated on the same gold film for comparison (Figure SI-1d, Figure SI-2d and Figure 6 inset SEM images). Each nanostructured square array was about 11.6 x 11.6 μm^2 with 17 slits in each array. Furthermore, square windows with the same opening area of the slit structures without DA NPs (Figure SI-1e) were fabricated (for instance, the 7.7 x 7.7 μm^2 S300-window matches the area of the S300-slit structure) as additional references (Figure SI-1f and Figure 6 inset SEM, Figure 7 bottom inset, Figure SI-2). Lastly, a 10 nm TiO_2 layer was e-beam evaporated on top of FIB-fabricated nanostructure to further tune the DA NPs SP resonance to the UC NPs excitation range. This TiO_2 spacer layer also minimize quenching due to the direct contact of emitters to metal surfaces.[32]

2.2 Materials and Sample Preparation

All chemicals were purchased from Sigma Aldrich and used without further purification. The UC NPs were prepared in chloroform (3% w/v) according to the previous published experimental procedure.[33, 34] A description of UC NPs synthesis is summarized in SI experimental section. Then, the UC NPs suspension was spin coated on the nanostructured gold film glass slide at 1200 revolutions per minute. This resulted in an UC NPs film with a thickness of 220 ± 20 nm. The film thickness was estimated from FIB cut cross sections of the sample following by SEM images near the nanostructured arrays. The film thickness was measured from the top of the Au film. Attempts to prepare films with thickness smaller than ~200 nm lead to heterogeneous coverage that included patches of UC NPs. Therefore, ~200 nm was the minimum thickness value that allowed a relatively homogeneous film.

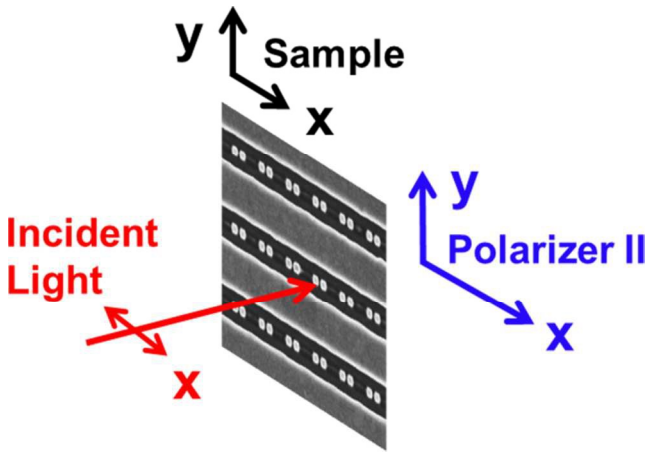

Figure 2 Schematic of the experimental configurations and definitions for UC emission measurements. Incident light polarization was fixed at normal incidence (red color); sample and polarizer II were rotated 90° accordingly for different types of measurements.

2.3 Instrumentation

The detailed experimental setup for the UC emission measurement is presented as supplementary information in Figure SI-3. The emission spectra were obtained under 980 nm continuous wave laser excitation with a fixed power density of

200 W/cm^2. The illumination area was about 100 μm^2 (shown in Figure 1d). The laser beam was incident normally onto the UC covered sample, then, the UC emission was collected at the back of the sample with an objective lens (20X, NA 0.4). This means that only the emissions transmitted through the nanostructures were measured. A spectrograph (HoloSpec VPT System from Kaiser) coupled to a CCD camera (DV-401-BV from ANDOR Technology) was used as a detection system (Figure SI-3). The sample orientation and light polarization directions were rotated accordingly to measure the UC emission spectra under different polarizations (Figure 2).

The white light transmittance for UC film-covered nanostructures were measured using a fiber (400 μm core diameter) coupled optical microscope (OLYMPUS MS PLAN ULWD 50X, NA 0.55 objective) with polarized light. A UV/VIS/NIR spectrometer (Ocean Optics 4000) was used as a detection system. SEM images were taken using a scanning electron microscope Hitachi S4800 at 1KV acceleration voltage.

2.4 FDTD simulations

FDTD simulations were performed using the Lumerical software housed at WestGrid (Western Canada Research Grid, part of Compute Canada national consortia for high performance computing) to visualize the electric field intensity profiles around the nanostructures. The dimensions of the nanostructures were based on the average measurements from the SEM images as mentioned above. A rectangular polygon with rounded corners was used to model the DA NPs. The dielectric properties of the gold and chromium were the default data reported by Johnson and Christy[35] and Palik[36] respectively, imported directly from the Lumerical material data base. Periodic boundary conditions were used in xy direction and with PML (perfect metal layers) in the ±z directions. Plane wave source was placed 1μm above Au nanostructures. The UC NP film refractive index[37] (n) was set as 1.50 above the Au metallic structure with 240 nm thickness assuming an uniform coverage; the glass substrate refractive index[36] (n) was imported from the Lumerical material data base. 10 nm TiO_2 dielectric layer was placed on top of Au slits bars, and the TiO_2 dielectric refractive index was obtained from the tabulated data.[38] An effective refractive index inside the slits was chosen as 1.85, considering non-uniform coverage of the UC NPs inside the slits, and a better transmittance agreement between the simulation and the experimental data. Near-field and transmission monitor were placed at the back of the nanostructures (12 nm and 1.3 μm away from the DA nanostructures, respectively). A 3 nm mesh size was used near the Au nanostructures.

3. Results and Discussion

The gold nanostructures were fabricated by FIB milling on 100 nm gold film. Figure 1a and b present SEM images of two slits arrays with 300 and 470 nm openings containing DA NPs with a gap distance of 30 nm (S300-G30 and S470-G30, respectively). Other arrays are shown in Figure SI-1 and SI-2 (see method section for the details). Figure 1c shows an SEM image of the UC NPs covering a nanostructured Au substrate. The SEM image indicates a relatively homogenous coverage with a random UC NPs (UC NPs diameter was ~ 30 nm) packed film on top of the nanostructured Au surface. Figure 1d presents an optical image of a gold film containing two nanostructured square arrays. The whole surface (including the nanostructures) was covered with UC NPs. One of the arrays in Figure 1d is illuminated by the laser, and the inset shows details of a dark field image under that laser illumination. Each square array in a given slide consisted of different nanostructures (as indicated above) and was excited individually using a 980 nm laser (illustrated by the bright spot in Fig. 1d). The UC emission from each array was collected under various excitation and collection configurations defined in Figure 2. The UC experimental measurement setup details are shown in Figure SI-3.

It is known that the light transmitted through a periodic slit structure strongly depends on its polarization.[2] The coupling of UC emissions to these polarization effects might be useful, for instance, in the generation of optical switches and polarization sensitive detectors.[39] In this work, the excitation polarization was fixed, but the relative orientation of the sample and polarizer II (Figure 2 and SI-3) was adjusted for different measurements. Figure 2 defines the four types of excitation/collection configurations: namely xxx, xxy, xyx, and xyy, respectively, where the first letter "x" defines the fixed incident light polarization (either white light or the 980 nm laser); the second letter either "x" or "y" defines the slits orientation relative to the incident polarization; and the third letter either "x" or "y" indicates the direction of polarizer II (analyzer) used in the measurement of the transmitted light through the sample oriented relative to the incident light polarization.

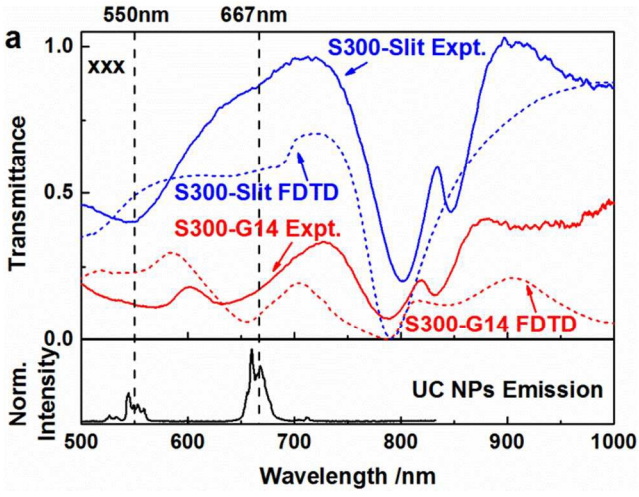

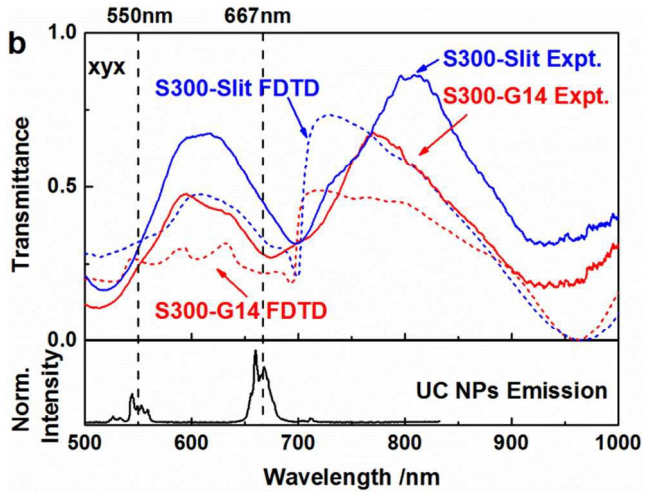

Figure 3 Experimental (solid lines) and FDTD calculated (dashed lines) xxx **(a)** and xyx **(b)** transmittance spectrum for S300-G14 DA and S300-Slit nanostructured arrays, respectively. A normalized UC emission spectrum from S300-window reference is added (black color) for comparison.

Before measuring the UC emission, each nanostructured array was characterized by polarized white light transmission (the same conditions as the laser excitation experiment, at normal incidence) to map the relative position of the resonances of the nanostructures relative to the UC NPs emission bands. Figure 3 presents examples of white light transmittance spectra, with xxx (Figure 3a) and xyx (Figure 3b) configurations, for the S300-G14 (300 nm slit width and 14 nm gap between the DA NPs) and S300-Slit array (the results for the other arrays are summarized in the SI, Figure SI-4), respectively. The transmittance spectra was calculated from the white light transmission spectra ($I^{WL}_{array}/I^{WL}_{window}$), where I^{WL}_{array} is the measured white light transmission from a nanostructured array, and I^{WL}_{window} is the measured white light transmission from the window reference (see Fig. SI-1f). An UC emission spectrum (for a UC NP film in glass excited at 980 nm) is also included in Figure 3 (black plot at the bottom of the figures) for comparison. FDTD calculations (dashed lines in Figure 3) were performed to provide additional insights in the optical processes. Due to the complicated nature of the systems investigated here, including the presence of fabrication defects; the possible variations in packing density for solid UC NPs films; the quality of the TiO_2 film; and the precise geometry of the metallic nanostructures;[40] an exact quantitative agreement between the experiments and simulations is not to be expected. However, the transmittance peaks/dips features predicted by FDTD qualitatively agree quite well with the experimental results. The experimental measurements (solid lines) in Figure 3 present a broadening of the features due to fabrication defects and measurement conditions. Normally, periodic nanoslits in gold film do not support strong white light transmission in the xxx configuration (transverse electric – TE polarization)[41, 42] However, the presence of a thin dielectric film coating the slit-only arrays enables significant white light transmission (blue lines in Figure 3) in that configuration (xxx), in agreement with reports from other groups (because the film supports waveguide modes).[43-45] Figure 3 illustrates that the UC green and red emission bands present different degrees of overlap with the transmittance spectrum, as expected (see dashed vertical lines in Figure 3).

The transmission spectrum of the S300-slit array under xxx configuration (Figure 3a) presents peaks near 700 and 900 nm. The peak near 700 nm is assigned by FDTD simulations to the Fabry-Perot (FP) direct cavity excitation mode (slit mode); while the peak near 900 nm is due to a surface wave coupled to the slit mode.[22, 41] Under the xyx configuration, Figure 3b, the two broad bands for the S300-Slit array (peaks near 600 and 800 nm) have similar assignments: the peak near 600 nm is a slit-cavity mode and the peak near 800 nm is a surface plasmon polariton (SPP) mode that assists the EOT (Figure SI-5). The presence of Au DA NPs inside the slits (Figure 3 S300-G14, red color) decreases the white light transmittance due to a combination of decreased opening area (~13%), increased back scattering, and absorption, compared to the slits without Au DA NPs (blue color). Most importantly, the EOT mechanism with additional nanostructures inside the nanoslits is different than for the slit-only nanostructures. The white light transmission from the slit structures containing DA NPs (S300 G14) present secondary peaks (additional peaks compared to slit-only nanostructures in Figure 3) that are related to the contributions of the DA plasmonic modes. The characteristics of all these different modes are further visualized in the numerical simulations presented in Figure 4.

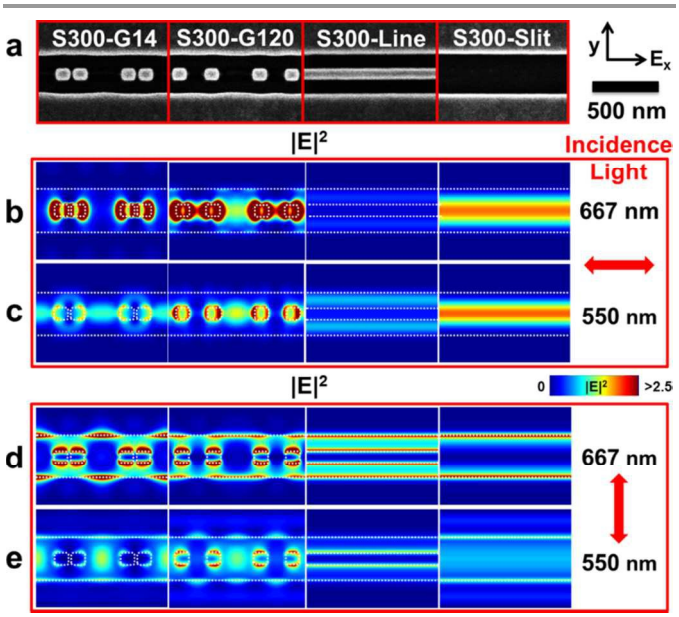

Figure 4 FDTD-calculated near field electric intensity ($|E|^2$) distribution for **(a)** S300-G14, S300-G120, S300-Line and S300-Slit nanostructures at the transmission position with the incidence light (red arrow) parallel **(b-c)** and perpendicular **(d-e)** to the nanoslits, respectively. The color scale is optimized to view the near field at different wavelengths (indicated beside the graph); the slit and DA NPs positions are outlined (white dashed lines).

The numerical calculations were performed considering infinite slits, since the length of the slits (11.7 μm) was much larger than the wavelengths (667 and 550 nm). FDTD-calculated

electric field profiles (at the position of the dashed lines in Figure 3, which correspond to the UC emission positions) for some of the nanostructures studied here are presented in Figure 4. Figure 4a presents the selected SEM images of the different types of arrays investigated (S300 set). The near electric field intensity distributions at the transmitted position (12 nm below the DA Au NPs) were plotted in Figure 4b-e for wavelengths at 667 nm (corresponding to the red UC emission) and 550 nm (green emission). The incident light was polarized either parallel or perpendicular to the slit (indicated as the red arrow on the right side in Figure 4). Figure 4b-e shows that different resonance modes are activated under different polarizations, and that the electric field intensity is distributed spatially differently around the nanostructures in the red and green spectral regions. These different polarization-dependent modes affect the characteristics of the transmitted UC, as will be demonstrated later. Plasmonic anisotropic dipolar antenna have been studied by several groups.[46-50] A clear anisotropic optical response was observed in those systems when using polarized light. Multipolar responses that depends on the dimensions of the antennas were also activated. The dimensions of the antennas in our experiments (~100 nm) indicate that the multipolar modes are expected for wavelength less than 500 nm. The multipolar near-field intensity is practically superimposed to the large dipolar plasmonic resonance. In this sense, the contribution to the photoluminescence enhancement (UC emission bands is at ~540 nm and ~ 650 nm) is likely dominated by the dipolar mode. Two major characteristics are observed from the numerical FDTD-calculations:

(1) The enhanced electric field intensity is concentrated near the Au NPs (in x direction) when light coupled to DA NPs in the parallel polarization direction (x-direction). In this case the DA "NP-NP gap mode" is activated (Figure 4 b and c). On the other hand, when light couples to the slit in perpendicular polarization (Figure 4d and e), the electric field is distributed along the y direction; concentrated in the gap between the lateral of the DA nanoparticles and the slit walls. In this case, a "DA-slit wall mode" is activated (Figure 4d and e).

(2) The magnitude of the local electric field intensity for red light is always greater than for the green electric field near the DA NPs for the particular geometries investigated here.

As for the S300-Line and S300-Slit samples, references without DA NPs inside (Figure 4b and c), an enhanced electric field is also observed for xxx polarization. The electric field in this case is centered on the slit gap, and, consequently, it is not bound to the metallic surface. This is characteristic to a FP-like interference within the thin dielectric film and the height of the slit structures (100 nm). On the other hand, when light is polarized perpendicular to the slit (Figure 4d and e), the "slit wall mode" is activated due to the excitation of high order SP modes since the zeroth order mode is excited at about 800 nm (Figure 3b transmittance spectrum). The SP modes overlapped better with the red emission than with the green under perpendicular polarization. In summary, the activation of the different modes ("NP-NP gap mode", "FP mode", and "DA-slit wall mode") are responsible for the polarization dependence of the observed white light transmittance features observed in Figure 3.

Figures 3 and 4 provided important insights into the EOT mechanisms through the nanostructures enabled by distinct optical modes. The effect of these modes on the transmitted UC will now be explored. As presented in the experimental section, the UC NPs were excited by a 980 nm laser, reaching the particles directly at normal incidence, and the UC emission was measured in transmission mode. It is assumed that each UC NP emits as a dipole source. The UC NPs film on top of the nanostructures was relatively thick (~200 nm), and the emission from that collective random distribution of dipoles can be considered, at a first approximation, as an un-polarized plane wave source travelling towards the nanostructured surface. This un-polarized UC emissions would have different transmissions in the x and y directions, as discussed above. A polarizer after the slit nanostructures (Figure 2 and Figure SI-3) allows the experimental evaluation of the enhanced UC emission transmitted at different polarizations (enabled by different resonance modes, as discussed in Fig. 4). Examples of UC emission transmitted spectra obtained with xyx orientation from some of the nanostructures are shown in Figure 5. The UC material exhibited characteristic green emissions ~530 nm and ~550 nm, assigned to the $^2H_{11/2} \rightarrow {}^4I_{15/2}$ and $^4S_{3/2} \rightarrow {}^4I_{15/2}$ transitions from Er^{3+} ions, respectively, and a red emission, ~665 nm, associated with the $^4F_{9/2} \rightarrow {}^4I_{15/2}$ Er^{3+} transition.[21, 33] In Figure 5, the red transmitted UC emission intensities are enhanced selectively for the different types of nanostructures, when compared to the window reference. The intensities of the transmitted emissions were dependent on the type of nanostructure and on the measurement configuration (polarization). A summary of the effect of the nanostructures in the UC emission is presented in the Figure 6 (emission intensities from the samples relative to the window reference for both the integrated green and red regions). The red emission was enhanced in all structures, but the slit structure presented the maximum (~ 6 fold) UC increase (relative to the window reference).

The enhanced transmitted UC emission is induced by the interactions between the UC NPs and the metallic nanostructures. Plasmonic-enhanced UC photoluminescence is often due to the UC NPs interaction with the enhanced local electric field near the metallic nanostructures.[21, 29, 51-53] In EOT, light is able to pass through metallic openings smaller than its wavelength mediated by SP resonance. The enhanced near electric field intensity should play then a significant role on both enhanced UC and transmission.[2, 29, 40, 53]

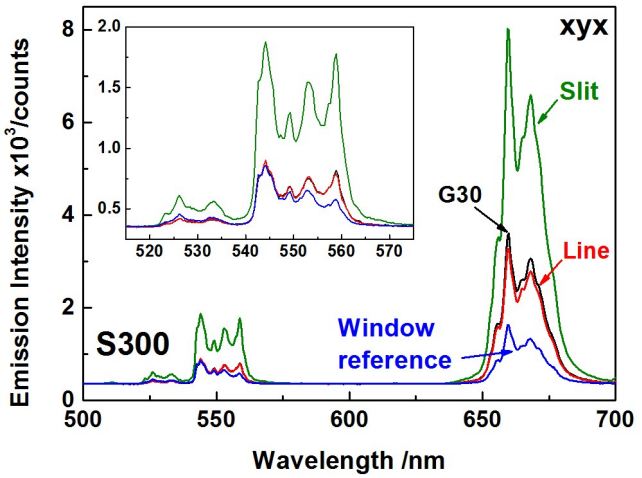

Figure 5 UC NPs emission spectra transmitted from different nanostructures (S300 set) as indicated in the figure. All the spectra were recorded under the same xyx condition.

The mechanism for plasmonic-enhanced UC generation could involve enhanced near field at both the excitation and the emission.[19, 21, 53] In terms of contributions from the near field enhancement at the excitation wavelength (980 nm), the experiments consistently demonstrated an increase in UC emission when the laser excitation was polarized perpendicular to the slits (higher enhancement for xyx compared to the xxx configurations for the S300-slit sample, for instance - see Figure 6). Considering that the direct laser excitation of the emitters in the film is polarization-independent, the preferential emission for when the incident polarization is crossed relative to the slit direction suggests the generation of resonant near field modes at the excitation energy that contributes to the enhanced UC generation (SPP-type, according to FDTD). The absolute UC for the samples containing DA inside the slits did not significantly change (for a particular polarization arrangement) with the gap distance between the metallic NPs (Figure 6), indicating that the NP-NP gap mode variation did not strongly affect neither the transmission nor the enhanced UC mechanism at those wavelengths. The largest absolute enhanced transmitted emission for the samples containing DA NPs was observed for the situations where the sample orientation was crossed with the analyzer (xyx and xxy configurations – see Figure 6). This also hints that the preferential mechanism for transmission in those cases is the DA - slit wall mode. The dominant role of the DA – slit wall mode over the DA NP – NP gap mode becomes even more evident when the results from a control sample containing only an Au line inside the slit (no gap) is analyzed. In this case, although significant UC transmission can be observed for the xyx and xxy configurations, a suppression in the UC transmission (relative to the window reference) is observed of the xxx and xyy arrangements (Figure 6). Hence, the line basically create a "double-slit" (see, for instance, Figures 4d,e), further selecting a preferential polarized transmission through that mode (light perpendicular to the slit is transmitted preferentially in those cases). In fact, the slit-Line samples presented the highest polarization dependence for enhanced UC emission EOT compared to all other nanostructures (see Figure SI-6). Figure SI-6 shows that S300-Line structure presents about 8 times polarization selectivity ($I_{xyx}^{UC\ red}/I_{xyy}^{UC\ red}$). The UC emission EOT is consistently polarized perpendicular to the slit direction for all nanostructures, since the polarization ratio is higher than unity in most cases (Figure SI-6). This effect corroborated the dominant role of "slit-like" modes in the enhanced transmission mechanism. Finally, the largest absolute enhancement in the transmitted UC was observed from the slit only sample (Figure 6). The FP mode (Figs. 4b,c) adds a significant contribution to the mechanism, enabling strong transmissions at xxx and xxy arrangements, while the slit surface mode (Fig. 4d) accounts for significant transmission at xyx and xyy.

The preceding discussion can be summarized as follows: The overall enhanced UC can be thought as two distinct processes for simplicity. One is the enhancement of the UC emissions, which is driven by local enhanced fields. Those can be enhanced fields at the excitation and at the emissions. The other process is the EOT, where the emissions transmitted through sub-wavelengths openings in the nanostructure are measured (at the emissions wavelengths). The experimental results for the slit case suggest that the enhancement in UC generation is driven by resonances at the excitation wavelength (Figure 3 and 5). In that case, both green and red UC emissions should have been equally enhanced; however, the relative amount of UC emissions (red and green) that preferentially transmit through the structures depend on the optical modes activated at those wavelengths. The independence of the amount of enhanced UC transmission with the DA NP-to-NP distance indicates that the DA NP-NP gap mode was not as significant for the enhanced transmission at those wavelengths, supporting the idea that the EOT is mainly driven by "slit-wall" modes.

The distribution of UC material inside the slit could also contribute to the decreased amount of emission in the presence of DA nanoparticles. This is because the S300-slit sample, for instance, contains a larger volume inside the opening to host UC materials in contact to the wall.

Another aspect to be considered is that the UC films in these experiments were relatively thick (~200 nm-thick films were necessary, in order to obtain an uniform coverage) compared to the typical decay distance of a plasmonic field. This means that not all UC NPs contributed to the overall enhancement in UC emission. In fact, stronger localization is observed for the DA NP-NP gap modes. The presence of the TiO_2 spacer should also influence the interaction of the SP field with the emitters in those cases. This helps to explain the independence of the UC emission with the NP-to-NP distance for those samples.

Since the film is relatively thick and only the UC NPs near to the surface are affected by the plasmonic field, the "real" enhancement factor (excluding the contributions from UC NPs that are away from the surface) should be larger than the experimental value reported here. Unfortunately, quantitative calculation of the fraction of the UC NPs that contributes to the

enhanced emission is not trivial. Some of the reasons are: the plasmonic field extension is wavelength-dependent; different resonance modes are involved for different polarizations; and different mechanisms involving both UC amplification and enhanced transmission through the nanostructures must be considered. However, it is possible to estimate an upper limit for the overall enhanced UC by considering that only the first layer of UC NPs (about 15% of the film) were strongly affected by the enhanced plasmonic near field at the excitation and that all enhanced UC were transmitted. Since the experimentally measured maximum enhanced UC emission was 6 times for the slit array (Figure 6, S300-Slit, red color), but only 15% of the film contributed to this enhancement (first layer of the film), then the upper limit of the enhancement factor, considering the assumptions discussed above, should be about 40 (again, measured against a window reference). It is important to emphasize that the slit resonances supports FP mode contributions (Figure 4b and c), which extends further into the film than the localized SP from the DA gap modes. This higher effective excitation certainly played an important role. In any case, the upper limit enhancement factor estimated here is in agreement with the UC enhancement enabled by plasmonic structures reported by other groups.[53] However, it is important to emphasize that in some cases the direct comparison of enhancement factors reported by different groups might be misleading due to several factors, including differences in experimental geometry. For instance, Zhang et al[30] has reported a 310-fold enhancement from 3D plasmonic nanoantennas. In that case, however, the experiments were realized in backscattering (reflection) mode and a glass substrate coated with the UC material was used as reference. Since both glass and the UC material are transparent in the visible (emission) range, and gold is a reflective metal, the ratio between the emission from the UC material on the plasmonic substrate and the emission from the UC material on a glass reference is bound to be a large number. This is in stark contrast to our experimental conditions, which requires the emission to be transmitted through a sub-wavelength aperture to be measured and used a window in a gold film as reference.

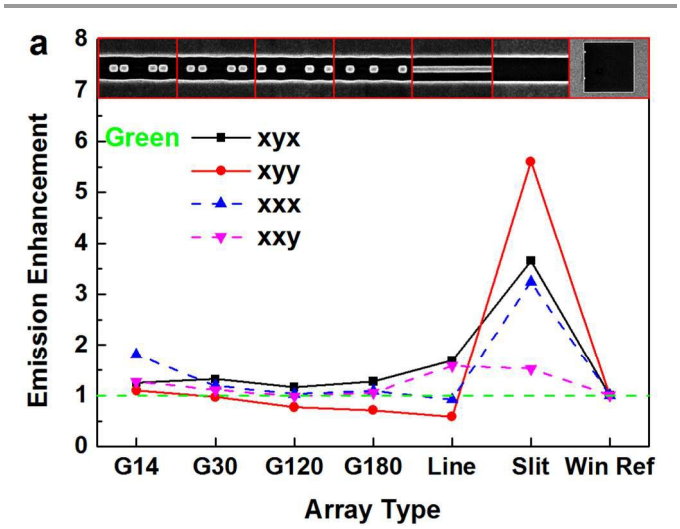

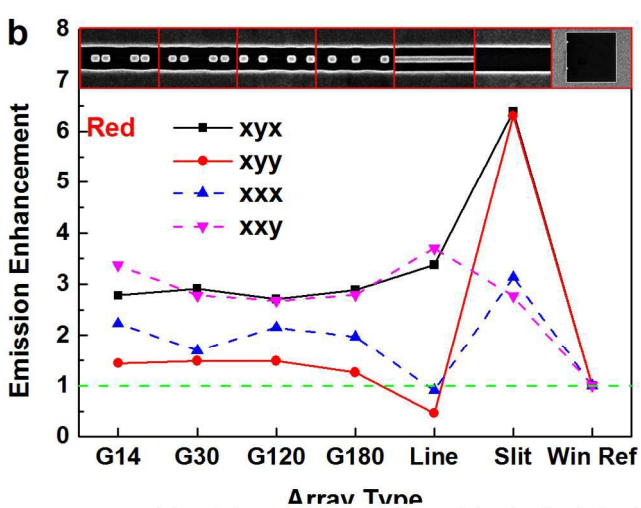

Figure 6 Summary of the relative enhancement of green **(a)** and red emission **(b)** using the window as reference for each array ($I^{UC}_{Structured}/I^{UC}_{Win\,ref.}$) with different measurement configuration (indicated on the graph). The emission intensities are corrected with the respective opening area for each type of array.

Another interesting observation is that the effect of the nanostructures (DA NPs and line) inside the slits led to tunable variations in the relative red and green UC transmitted emission intensity ($I^{UC}_{Red}/I^{UC}_{Green}$). The relative intensity ratios ($I^{UC}_{Red}/I^{UC}_{Green}$, green: integrated from 520 nm to 570 nm, red: integrated from 640 nm to 690 nm) were calculated and plotted in Figure 7a. Figure 7a shows a polarization dependent tunable preferential enhancement of the red UC transmitted emission for the nanostructured arrays compared to the window reference. The presence of the Au DA nanostructures insides the slits (S300-G14 to G180) induces even higher preferential enhanced red UC transmitted emission relative to green emission compared to the slit only (S300-Slit) structure. As for the window reference, there are no polarization dependence ($I^{UC}_{Red}/I^{UC}_{Green}$ = ~2.5) as expected.

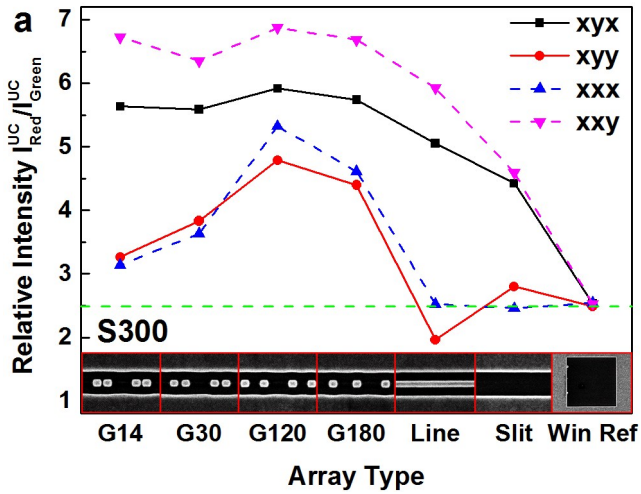

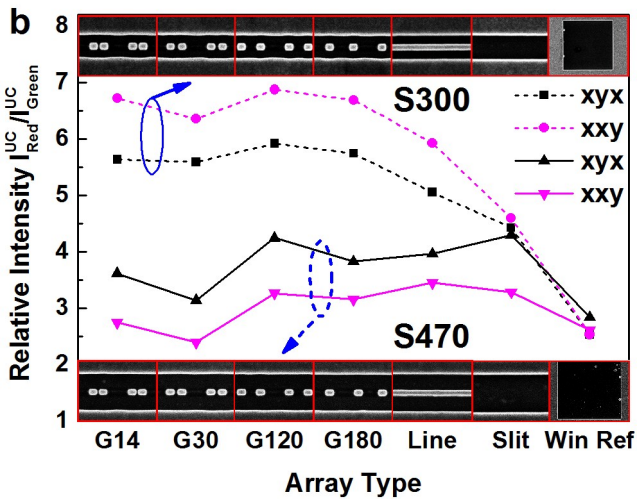

Figure 7 (a) Relative integrated UC emission intensity ratio between the red (from 640 nm to 690 nm) and the green (from 520 nm to 570 nm) emission ($I^{UC}_{Red}/I^{UC}_{Green}$) for each nanostructured S300 array under different measurement configurations (indicated in the figure) **(b)** Comparison of the tunable feature of the relative UC emission between the red (from 640 nm to 690 nm) and the green (from 520 nm to 570 nm) emission ($I^{UC}_{Red}/I^{UC}_{Green}$) with a large slit (S470, solid lines) and the narrow slits (S300, dashed lines) for each nanostructured array are presented.

As discussed above, the observed UC emissions show strong polarization dependence through the activation of the different EOT modes. The free-space light and SP resonance mode coupling efficiency[30, 54] often affects the EOT intensities. Both experimental and FDTD-calculated results indicate an enhanced red light relative to the green light as expected. It is then suggested that preferential enhanced $I^{UC}_{Red}/I^{UC}_{Green}$ emission is due to a dominant role of the "DA-slit wall mode". This assumption can be tested by increasing the slit width, which should consequently decrease the theoretical slit mode SP resonance coupling efficiency,[53, 54] hence, affecting the UC emissions EOT intensities. Figure 7b presents experimental results of the relative enhanced UC emission with the same set of nanostructures as S300 arrays (dashed lines, Figure 7b SEM inset on the top) but a large slits nanostructures (S470 and Figure SI-2) and a large window reference (solid line, Figure 7b SEM inset on the bottom) on the same substrate. The preferential enhanced red emission ($I^{UC}_{Red}/I^{UC}_{Green}$) was indeed significantly lowered for the larger slit (S470) width when compared to the narrow nanoslits (S300). This can be rationalized by considering that the "DA-slit wall mode" interaction blue shifts with the increase of the NP-wall distance, favoring an increase in the green UC emission relative to the red.

4. Conclusions

The enhanced upconversion (UC) emission through plasmonic interactions between $NaYF_4$:Yb/Er and gold nanostructures was investigated. The UC transmission presented a polarization effect, tuned by the plasmonic nanostructures. In general, a preferential enhancement of the red emission over the green UC emission was observed for all nanostructures (double antenna nanoparticles and lines) nested in two kinds (300 and 470 nm slit opening) of nanoslits. FDTD-calculations suggest that the UC enhancement and the polarization effects in the transmitted EOT resulted from different electric field modes activated by different excitation arrangements. The relative intensity, I_{650nm}/I_{540nm}, measured for the emission transmitted through the nanostructures and their dependence with polarization conditions acted as a probe of surface plasmon modes contribution to the EOT. Although the geometric parameters of the double-antennas (gap distance) allowed some tuning of the optical properties of the nanostructures, they did not have a strong effect on the overall UC enhancement measured experimentally. This might be related to several effects, including the sample volume probed by the highly localized field at the gaps and the presence of a TiO_2 spacer in the samples, which separated the UC sample from the region of higher localized field at the surface.

Acknowledgements

This work was supported by the National Science and Engineering Research Council (NSERC) of Canada; UVic Advanced Microscopy Facility and the authors would like to thank Reuven Gordon for help with the FDTD simulations.

Notes and references

[a] University of Victoria, Department of Chemistry P.O. Box 3065, Stn CSC, Victoria, BC V8W 3V6 Canada.
[b] Laboratório de Microeletrônica, Departamento de Engenharia Elétrica, Escola Politécnica, Universidade de São Paulo, Av. Professor Luciano Gualberto, 158 trav.3, no. 158,São Paulo 05508-900, SP, Brazil.
[†] Electronic Supplementary Information (ESI) available: SEM images, experiment setup, white light transmittance spectra, FDTD simulation result for the transmission mode and polarization intensity ratio for UC emission. See DOI: 10.1039/b000000x/

1. P. Lalanne, J. P. Hugonin and J. C. Rodier, *Phys. Rev. Lett.*, 2005, **95**, 263902.
2. M. J. Kofke, D. H. Waldeck and G. C. Walker, *Opt. Express*, 2010, **18**, 7705-7713.
3. R. Gordon, A. G. Brolo, D. Sinton and K. L. Kavanagh, *Laser & Photonics Reviews*, 2010, **4**, 311-335.
4. F. J. Garcia-Vidal, L. Martin-Moreno, T. W. Ebbesen and L. Kuipers, *Rev. Mod. Phys.*, 2010, **82**, 729-787.
5. J. Weiner, *Rep. Prog. Phys.*, 2009, **72**, 064401.
6. T. W. Ebbesen, H. J. Lezec, H. F. Ghaemi, T. Thio and P. A. Wolff, *Nature*, 1998, **391**, 667-669.
7. A. G. Brolo, *Nat Photon*, 2012, **6**, 709-713.
8. L. Chrostowski, *Nat Photon*, 2010, **4**, 413-415.
9. T. Søndergaard, S. I. Bozhevolnyi, S. M. Novikov, J. Beermann, E. s. Devaux and T. W. Ebbesen, *Nano Lett.*, 2010, **10**, 3123-3128.
10. V. E. Ferry, J. N. Munday and H. A. Atwater, *Adv. Mater.*, 2010, **22**, 4794-4808.
11. T. Gao, B. Wang, B. Ding, J.-k. Lee and P. W. Leu, *Nano Lett.*, 2014, **14**, 2105−2110.
12. C. A. Ashwin, G.-E. Aitzol, A. Hadiseh and A. D. Jennifer, *Journal of Optics*, 2012, **14**, 024008.
13. J. Pichaandi, J.-C. Boyer, K. R. Delaney and F. C. J. M. van Veggel, *J. Phys. Chem. C*, 2011, **115**, 19054-19064.
14. C. Shi, S. Soltani and A. M. Armani, *Nano Lett.*, 2013, **13**, 5827-5831.

15. W. van Sark, J. de Wild, J. Rath, A. Meijerink and R. E. Schropp, *Nanoscale Research Letters*, 2013, **8**, 81.
16. Z. Zhou, J. Wang, F. Nan, C. Bu, Z. Yu, W. Liu, S. Guo, H. Hu and X.-Z. Zhao, *Nanoscale*, 2014, **6**, 2052-2055.
17. V. A. G. Rivera, F. A. Ferri and E. M. Jr., *Localized Surface Plasmon Resonances: Noble Metal Nanoparticle Interaction with Rare-Earth Ions*, 2012.
18. F. Auzel, *Chem. Rev.*, 2004, **104**, 139-173.
19. Q. Luu, A. Hor, J. Fisher, R. B. Anderson, S. Liu, T.-S. Luk, H. P. Paudel, M. Farrokh Baroughi, P. S. May and S. Smith, *J. Phys. Chem. C*, 2014, **118**, 3251-3257.
20. Q.-C. Sun, H. Mundoor, J. C. Ribot, V. Singh, I. I. Smalyukh and P. Nagpal, *Nano Lett.*, 2013, **14**, 101-106.
21. D. M. Wu, A. García-Etxarri, A. Salleo and J. A. Dionne, *J. Phys. Chem. lett.*, 2014, **5**, 4020-4031.
22. C. L. Nathan, N. Prashant, M. M. Kevin, J. N. David and O. Sang-Hyun, *Rep. Prog. Phys.*, 2012, **75**, 036501.
23. N. Livneh, A. Strauss, I. Schwarz, I. Rosenberg, A. Zimran, S. Yochelis, G. Chen, U. Banin, Y. Paltiel and R. Rapaport, *Nano Lett.*, 2011, **11**, 1630-1635.
24. T. Zhang and F. Shan, *Journal of Nanomaterials*, 2014, **2014**, 16.
25. H. Aouani, M. Rahmani, M. Navarro-Cia and S. A. Maier, *Nat Nano*, 2014, **9**, 290-294.
26. H. Aouani, O. Mahboub, E. Devaux, H. Rigneault, T. W. Ebbesen and J. Wenger, *Nano Lett.*, 2011, **11**, 2400-2406.
27. T.-H. Wong, J. Yu, Y. Bai, W. Johnson, S. Chen, M. Petros and U. N. Singh, *OPTICE*, 2014, **53**, 107102-107102.
28. L. Ma, O. Slattery and X. Tang, *Phys. Rep.*, 2012, **521**, 69-94.
29. E. Verhagen, L. Kuipers and A. Polman, *Opt. Express*, 2009, **17**, 14586-14598.
30. W. Zhang, F. Ding and S. Y. Chou, *Adv. Mater.*, 2012, **24**, OP236-OP241.
31. K. Thyagarajan, S. Rivier, A. Lovera and O. J. F. Martin, *Opt. Express*, 2012, **20**, 12860-12865.
32. L. Qi, C. Yanrui, L. Zhiqiang, Z. Feng, C. Xiaohong, S. Zhuo, W. Yunle, G. Hai, W. Zeng Bo and H. Sumei, *Nanotechnology*, 2014, **25**, 185401.
33. N. J. J. Johnson, N. M. Sangeetha, J.-C. Boyer and F. C. J. M. van Veggel, *Nanoscale*, 2010, **2**, 771-777.
34. J.-C. Boyer, M.-P. Manseau, J. I. Murray and F. C. J. M. van Veggel, *Langmuir*, 2009, **26**, 1157-1164.
35. P. B. Johnson and R. W. Christy, *Phys. Rev. B*, 1972, **6**, 4370-4379.
36. E. D. Palik, *Handbook of optical constants of solids*, Acad. Press, Boston u.a., 1997.
37. S. Fischer, H. Steinkemper, P. Löper, M. Hermle and J. C. Goldschmidt, *J. Appl. Phys.*, 2012, **111**, 013109.
38. J. R. Devore, *J. Opt. Soc. Am.*, 1951, **41**, 416-417.
39. J. Wang, M. S. Gudiksen, X. Duan, Y. Cui and C. M. Lieber, *Science*, 2001, **293**, 1455-1457.
40. Y. Liang, W. Peng, R. Hu and H. Zou, *Opt. Express*, 2013, **21**, 6139-6152.
41. D. Zhang, P. Wang, X. Jiao, C. Min, G. Yuan, Y. Deng, H. Ming, L. Zhang and W. Liu, *Appl. Phys. B*, 2006, **85**, 139-143.
42. I. Schwarz, N. Livneh and R. Rapaport, *Opt. Express*, 2012, **20**, 426-439.
43. S. Zhijun, G. Tengpeng, C. Wei and Z. Xiaoliu, *Applied Physics Express*, 2014, **7**, 032001.
44. M. Esteban, L. Martín-Moreno and F. J. García-Vidal, *Journal of Optics A: Pure and Applied Optics*, 2006, **8**, S94.
45. M. Guillaumée, A. Y. Nikitin, M. J. K. Klein, L. A. Dunbar, V. Spassov, R. Eckert, L. Martín-Moreno, F. J. García-Vidal and R. P. Stanley, *Opt. Express*, 2010, **18**, 9722-9727.
46. V. A. Podolskiy and E. E. Narimanov, *Phys. Rev. B*, 2005, **71**, 201101.
47. G. Schider, J. R. Krenn, A. Hohenau, H. Ditlbacher, A. Leitner, F. R. Aussenegg, W. L. Schaich, I. Puscasu, B. Monacelli and G. Boreman, *Phys. Rev. B*, 2003, **68**, 155427.
48. W. L. Schaich, G. Schider, J. R. Krenn, A. Leitner, F. R. Aussenegg, I. Puscasu, B. Monacelli and G. Boreman, *Appl. Opt.*, 2003, **42**, 5714-5721.
49. G. Schider, J. R. Krenn, W. Gotschy, B. Lamprecht, H. Ditlbacher, A. Leitner and F. R. Aussenegg, *J. Appl. Phys.*, 2001, **90**, 3825-3830.
50. J. R. Krenn, G. Schider, W. Rechberger, B. Lamprecht, A. Leitner, F. R. Aussenegg and J. C. Weeber, *Appl. Phys. Lett.*, 2000, **77**, 3379-3381.
51. S. Schietinger, T. Aichele, H.-Q. Wang, T. Nann and O. Benson, *Nano Lett.*, 2009, **10**, 134-138.
52. H. Zhang, Y. Li, I. A. Ivanov, Y. Qu, Y. Huang and X. Duan, *Angew. Chem. Int. Ed.*, 2010, **49**, 2865-2868.
53. D. Lu, S. K. Cho, S. Ahn, L. Brun, C. J. Summers and W. Park, *ACS Nano*, 2014, **8**, 7780-7792.
54. R. Mehfuz, M. W. Maqsood and K. J. Chau, *Opt. Express*, 2010, **18**, 18206-18216.